The Sensitivity of West African Squall Line Water Budgets to Land Cover

Karen I. Mohr[1], R. David Baker[2], Wei-Kuo Tao[3], and James S. Famiglietti[4]

[1]*Department of Earth and Atmospheric Sciences*
University at Albany, SUNY
Albany, NY 12222

[2]*Physics Department*
Austin College
Sherman, TX 75090

[3]*Laboratory for Atmospheres*
NASA/Goddard Space Flight Center
Greenbelt, MD 20771

[4]*Department of Earth System Science*
University of California, Irvine
Irvine, CA 92697-3100

Submitted to *Journal of Hydrometeorology*, August 2001

Corresponding Author
Karen I. Mohr
Department of Earth and Atmospheric Sciences
University at Albany, SUNY
Albany, NY 12222
Voice: (518) 442-4561
Fax: (518) 442-5825
mohr@atmos.albany.edu

Abstract

This study used a two-dimensional coupled land/atmosphere (cloud-resolving) model to investigate the influence of land cover on the water budgets of squall lines in the Sahel. Study simulations used the same initial sounding and one of three different land covers, a sparsely vegetated semi-desert, a grassy savanna, and a dense evergreen broadleaf forest. All simulations began at midnight and ran for 24 hours to capture a full diurnal cycle. In the morning, the latent heat flux, boundary layer mixing ratio, and moist static energy in the boundary layer exhibited notable variations among the three land covers. The broadleaf forest had the highest latent heat flux, the shallowest, moistest, slowest growing boundary layer, and significantly more moist static energy per unit area than the savanna and semi-desert. Although all simulations produced squall lines by early afternoon, the broadleaf forest had the most intense, longest-lived squall lines with 29% more rainfall than the savanna and 37% more than the semi-desert.

The sensitivity of the results to vegetation density, initial sounding humidity, and grid resolution was also assessed. There were greater differences in rainfall among land cover types than among simulations of the same land cover with varying amounts of vegetation. Small changes in humidity were equivalent in effect to large changes in land cover, producing large changes in the condensate and rainfall. Decreasing the humidity had a greater effect on rainfall volume than increasing the humidity. Reducing the grid resolution from 1.5 km to 0.5 km decreased the temperature and humidity of the cold pools and increased the rain volume.

Introduction

Highly variable rainfall and highly variable, but principally sparse, vegetation characterize the West African Sahel. Mesoscale convective systems (MCS) are organized, multi-cellular convective cloud clusters with an area extent on the order of 1000 km^2 and a lifetime of 6 or more hours. MCSs contribute a majority of the wet season rainfall in the Sahel, even though they constitute fewer than 20% of the total precipitating cloud clusters (Mohr et al. 1999; Nesbitt et al. 2000). In Nicholson (1988), the difference between wet and dry years is more strongly correlated to the number of days with rainfall greater than 40 mm than the total number of rainfall days.

A "squall line" is an MCS in which the cumulonimbus clouds are arranged linearly. In West Africa squall lines range from 100–1000 km in length, are oriented north-south perpendicular to the mean flow, travel westward, and live for 6 hours or more. Censuses of West African squall lines (Aspliden et al. 1976; Rowell and Milford 1993; Hodges and Thorncroft 1997) give the basic ingredients for their formation as low- to mid-tropospheric vertical shear, low-level convergence, and low-level potential instability. The African easterly jet at 650–700 mb is the result of regional temperature and humidity differences across northern Africa. The vertical and horizontal shears associated with the African easterly jet contribute directly and indirectly to the first two ingredients of squall line development.

Wet season boundary layer temperature and humidity profiles are governed by the intrusion of humid air in the summer monsoon and the contribution from land surface evapotranspiration. Soil water content and land cover govern evapotranspiration and the flux of energy and water vapor to the boundary layer. Variability in the latent heat flux may thus suppress or enhance moist convection locally. Crook (1996) and Lucas et al. (2000) have

investigated the possible sensitivity of convection to environmental humidity by using cloud-resolving models. Both studies found noticeable increases in the amount of rainfall with small increases in boundary layer humidity. In Crook's (1996) study, changes in the boundary layer humidity on the order of observational error, 1 g kg^{-1}, made the difference between no initiation and intense convection. Can surface fluxes in a semi-arid region such as the Sahel influence the characteristics of the boundary layer enough to produce significant changes in MCS development?

This study investigates how land cover may influence squall line water budgets in the Sahel (Figure 1). Currently, grassy savanna constitutes the majority of the area in the box in Figure 1 and supports millet cultivation and livestock grazing. From satellite observations of Sahelian land cover, changes in vegetation density are closely correlated with interannual fluctuations in rainfall, although human activity may exacerbate ecosystem changes, particularly during dry years (Nicholson et al. 1998). Hence, agricultural productivity and aquifer recharge will depend greatly on the size and other characteristics of wet season MCSs. Brubaker et al. (1993) have shown that precipitation recycling approaches 50% in West Africa in the summer, implying an important role for the land surface in rainfall development. In this study, we concentrate on examining the physical links between surface/boundary layer processes and their affect on convective clouds.

Hydrometeorological modeling permits us to control inputs and measure outputs in land/atmosphere interaction quantitatively. The purpose is not to simulate a particular squall line event as in a case study but to examine how model squall lines develop in different environments and isolate the factors that may be responsible for measurable differences in their water budgets. Previous studies using cloud-resolving models to simulate MCSs in West Africa have prescribed

surface fluxes rather than an interactive land surface (Dudhia et al. 1987; Lafore and Moncrieff 1989; Chang and Yoshizaki 1993). We use a coupled, fully interactive land/atmosphere (cloud-resolving) model to compare system development over three different land covers representative of major biomes in West Africa (map in Figure 1), the grassy savanna and semi-desert biomes of the Sahel and the evergreen broadleaf forest biome near the southern edge of the Sahel. Since precipitation from an MCS is a function of system size, structure, and longevity, precipitation and associated variables in the water budget (e.g., condensation and evaporation) will be the key results used to evaluate differences among simulations.

Methods

a. Numerical model

The simulations for this study used a two-dimensional (2D) coupled land/atmosphere (cloud-resolving) numerical model with open lateral boundary conditions. Goddard Cumulus Ensemble (GCE) is a non-hydrostatic, anelastic numerical cloud-resolving model composed of prognostic equations for momentum, potential temperature, and water vapor mixing ratio (Tao and Simpson 1993). The GCE includes solar and infrared radiative transfer processes, a Kessler-type two-category (cloud drops and rain) liquid water scheme, and a three-category (cloud ice, snow, and graupel/hail) ice microphysics schemes (Lin et al. 1983; Rutledge and Hobbs 1984). For our simulations of tropical convection, we chose graupel as our third class of ice particles. Coupled to GCE is the Parameterization for Land-Atmosphere-Cloud Exchange (PLACE), a surface-vegetation-atmosphere transfer model (Wetzel and Boone 1995). PLACE consists of linked process models (e.g., net radiation, evapotranspiration, ground heat storage) and emphasizes the vertical transport of moisture and energy through the 5 layer soil moisture and the 7 layer soil temperature column to the overlying heterogeneous land surface. The exchange

of radiation and heat, momentum, and moisture fluxes couple the GCE and PLACE models (Tao et al. 2001). Lynn et al. (1998) and Baker et al. (2001) have used GCE-PLACE to simulate landscape-generated and sea breeze-generated deep convection.

A computationally efficient 2D model such as GCE-PLACE is an attractive choice, supported by the results of previous studies that show that the mean kinematic and thermodynamic properties of a squall line are well simulated in 2D models (Nicholls et al. 1988; Ferrier et al. 1996; Tao et al. 1996; Xu and Randall 1996; Grabowski et al. 1998; Lucas et al. 2000). The simulation of horizontal circulation features, momentum transports, and other inherently three-dimensional features of squall line dynamics would be more appropriately handled with three-dimensional models. In this study we focus on the mean and cumulative values of surface precipitation and other variables in the water budget. Because we are using a coupled land/atmosphere model, we will also consider selected surface and sub-surface hydrologic variables. A 2D model is appropriate for exploring the sensitivity of area-average thermodynamic and hydrologic variables to changes in the surface environment. The computational efficiency of a 2D model becomes especially advantageous when simulating a large area at a fine resolution.

The grid used in the simulations was a transect of approximately 1000 km divided into 2048 grid points with 1990 inner points at 0.5 km spacing and a stretched (1:1.06) grid on either side. Vertically, there were 33 grid points from 0.0 to 21.5 km altitude. The grid was stretched, with spacing between levels ranging from 80 m at the surface to 1200 m at the top of the troposphere. Stretching in the vertical increases computational efficiency without significantly compromising accuracy (Weisman et al. 1997). Boundary conditions were open lateral. The

GCE time step was 5 s, and GCE invoked PLACE in 3 min intervals. All simulations began at local midnight and ran for 24 hours.

b. Initial conditions

Because this study examines the sensitivity to land surface conditions, the initial atmospheric profile is the same for all simulations. The sounding (Figure 2) is from a pre-storm environment, 23 June 1981 at 2335 Z, during the *Convection Profonde Tropicale* (COPT81) field experiment in an area straddling the Ivory Coast and Burkina Faso (Chalon et al. 1988; Roux 1988). The sounding used in the simulations is depicted in Figure 2. The African Easterly Jet is detectable in the winds around 600 mb, providing strong low to mid-level vertical shear. Typically, cloud modelers rely on lifting from a warm bubble or a cold pool to initiate convection. To isolate the sensitivity of convective initiation and development to land surface conditions, we do not apply a lifting mechanism, relying instead on the high potential instability of the 23 June COPT81 sounding and surface heating gradients to initiate convection.

The initial surface conditions define the simulations used in this study. There are three land covers, semi-desert (scrub), savanna, and evergreen broadleaf forest, described in Table 1. The semi-desert landcover is sparse, deeply rooted, highly reflective, and tolerant of high temperatures. The savanna and broadleaf forest land covers are noticeably thicker as well as taller, and most of the roots are higher in the soil column than in the semi-desert. We will make frequent use of the abbreviations in Table 1 in referring to each simulation.

All grid points in all of the simulations were assigned sandy loam soil, a common soil type in the region. Although this assumption simplifies the natural variability of soil types in the region, Mohr et al. (2000) have shown that PLACE's sensitivity to soil type can overwhelm any signal from vegetation characteristics. To isolate sensitivity to vegetation, it thus became

necessary to specify the same soil type for all simulations. Each vegetation type had its own initial soil moisture and soil temperature profiles. We created a first guess soil moisture profile (Table 1) with random perturbations of 2–6% and no moisture gradient. The first guess soil temperature profile was 298 K at the eastern and western boundaries with a peak soil temperature of 300 K at 600 km to encourage convective initiation near but not on the western boundary. To create unique, steady state profiles for each land cover type, we assigned one of the three land covers to the PLACE gridcells, applied the first guess soil moisture and soil temperature profiles, ran PLACE off-line for several hours, and then iterated the simulation until there was no change in the profiles. To reach steady state, about 50 iterations were required. Differences in the initial soil moisture (Table 1) and soil temperature profiles are small, so that the principal difference among the simulations is the assigned vegetation type and density.

Results

a. Heat fluxes and boundary layer energy

The time series of surface fluxes are plotted in Figure 3. Figure 3a is the area-average difference between net radiation and ground heat flux ($R_{net} - G$) for the SD, SAV, and FOR simulations. The comparison of net radiation to the ground heat flux indicates the fraction of radiation conducted into the soil versus the fraction available to affect the diurnal cycle of low-level equivalent potential temperature (θ_e) and thus moist entropy (Betts and Ball 1995, 1998). Mid-day, there is 15% more available energy in the FOR simulation than in the SAV simulation and 30% more than the SD simulation. Enhanced ground heat flux causes the SD soil temperatures to increase more rapidly than the FOR soil. The SD average 10-cm soil temperature increases 9 K and the skin temperature increases 24 K over 6 hours (8:00–14:00).

For the same period in the FOR, the 10-cm soil and skin temperatures increase 4 K and 12 K, respectively.

The differences in sensible and latent heat fluxes among simulations are even larger. The midday sensible heat flux (Figure 3b) in the SD and SAV is nearly double that of the FOR. In Figure 3c there are two peaks in the latent heat flux. Evapotranspiration produces the first peak in the morning, but the second peak in the afternoon has a large contribution from evaporating rainfall. The difference at each peak between the FOR and the SAV and SD is larger in the morning (50% and 75%, respectively) than in the mid-afternoon (30% and 35%). For PLACE, latent heat flux is determined by plant physiology, available moisture, and atmospheric demand. High morning soil temperatures, as in the SD simulation, will suppress evapotranspiration, increase the sensible heat flux, and may establish a negative feedback between soil temperature and additional evapotranspiration (Mohr et al. 2000). The SAV and FOR have comparable amounts of available energy. The simulated patchy grass and woody shrubs of the SAV converted less available energy to latent heat flux than the dense cover of broadleaf trees in the FOR. Even though there is less energy ($R_{net} - G$) available to the SD than the SAV, most of the available energy in the sparsely vegetated SD was converted into sensible heat flux until mid-afternoon.

The moist static energy (MSE), or moist entropy, in the boundary layer is the sum of the potential energy, sensible heat energy, and latent heat energy: $MSE = gz + C_pT + Lw$. Here, g is the gravitational acceleration, z elevation, C_p specific heat capacity at constant pressure, T temperature, L latent heat of vaporization, and w water vapor mixing ratio. Of these terms, the sensible heat term is the largest, on the order of 10^5 J kg^{-1}, and the latent heat term an order of

magnitude smaller[1]. A significant vertical gradient of MSE encourages the development of moist convection to re-establish a neutral vertical distribution. Although convective available potential energy (CAPE) is commonly used to assess the potential for deep convection, MSE is easily related to surface fluxes and is useful for diagnosing the thermodynamic state and buoyancy of the boundary layer. Later, CAPE will be used in evaluating convective intensity.

Because the sensible heat term dominates the calculation of MSE, the total MSE in the lowest 2 km varies only 2% among the simulations. Since total MSE is of limited use, we consider how *MSE per unit area in the boundary layer* changes during the day. Figure 4a is the time series of boundary layer growth. The curves are not smooth since the heights are diagnosed from discrete model layers. Until sunset, the FOR has the shallowest, slowest growing boundary layer. Morning boundary layer growth in the SAV is slightly slower than the SD, but their boundary layers attain the same maximum heights. Figures 4b-c track the changes in MSE and mixing ratio per unit area. The MSE per unit area in Figure 4b is the sum of the MSE in the gridcells in the boundary layer divided by the area under the top of the boundary layer. In the morning, the FOR (Figure 4b) has 30% more MSE per unit area than the SD and 20% more than the SAV. The SAV has 15% more MSE per unit area than the SD but less than 1% more in the afternoon. Only after sunset does the difference between the FOR and the other simulations begin to close. Because all simulations used the same initial sounding, the boundary layer average mixing ratio (Figure 4c) of the simulations is the same for the first 3 hours and within 0.6 g kg^{-1} until mid-morning. From mid-morning to sunset, the mixing ratio in the shallower FOR boundary layer is consistently 2–3 g kg^{-1} (~ 20%) higher than the SAV and SD.

[1] Assuming a surface temperature around 300 K, the MKS values for C_p and L, and mixing ratio of 10^{-2} kg kg^{-1}.

Related to the MSE per unit area is the vertical gradient of MSE. It is easier to diagnose the vertical gradient of MSE by using θ_e as a proxy. In Figure 5, the FOR has the deepest layer of air with θ_e greater than 348K, and much of the surface layer is greater than 351K. The SAV has a shallower layer greater than 348K and no contoured areas above 350K. The SD has only isolated patches greater than 348K. In all three simulations, θ_e is less than 335K by 2 km, but the vertical gradient of θ_e below 2 km is greater in the FOR simulation.

b. Cloud and system development

Figure 6 is the time series of total hydrometeor content. Enhanced cumulus and rainfall begin by 12:00 in the SD and SAV and 13:00 in the FOR. In Figure 3c, the latent heat flux at 12:00 is still increasing in the FOR. The later onset of deep convection in the FOR allowed extra time for surface fluxes to strengthen the vertical gradient of θ_e. Peak cloud coverage occurs an hour after initiation of rainfall in the three simulations, then decreases after peaking. Around 18:00, a second, although smaller, peak in cloud cover occurs in the FOR but not in the SD or SAV simulations.

Squall lines develop in all three simulations, although there are marked differences with respect to convective intensity, longevity, and rainfall. In Figure 7 are *x-t* plots of rainfall. In each simulation, several of the cumulonimbus clusters develop cold pools and propagate eastward as squall lines, although the longest-lived squall lines initiated on the east side of the transect. The SD simulation has the fewest and shortest-lived squall lines. A few more cumulonimbus clusters form in the SAV, and the squall lines last longer than in the SD. Rainfall ceases in the SD and SAV simulations by 17:00 and 18:00, respectively. The FOR simulation has several squall lines that last as long as or longer than the longest lasting squall lines in the SD and SAV. The FOR squall lines initiating near 600 km last until the last half hour of the

simulation period, about 10 hours in total. Table 2 compares the percent difference in area (the contoured areas in Figure 7) for several rain rates. The SAV has only 9% more raining area than the SD, but FOR has almost twice the raining area of the other simulations. The difference in area between the FOR and the other simulations decreases with rain rate although it is still significant.

To assess convective intensity, Figures 8a-b are the time series of maximum vertical velocity and maximum rain rate. The maximum vertical velocities and rain rates generally correlate, with the strongest vertical velocities (i.e., most intense convection) and heaviest rainfall occurring in the first 2 hours after initiation. The highest vertical velocities and rain rates also occur in the FOR simulation, although they occur as isolated events. Except for a spike greater than 400 mm hr^{-1} (Figure 8b) in FOR, the magnitudes of the maximum rain rates between 12:00–15:00 are comparable.

Even more than convective intensity, the most important difference among the simulations is the longevity of organized convection. The SAV and FOR simulations, but not the SD, have a second period of strong development (16:00 and 18:00, respectively) but it is shorter than the first period. The second period of development (18:00) in the FOR coincides with the final dissipation of the SD and SAV squall lines. From Figures 6–8 and Table 2, the SAV simulation produced slightly more deep convection compared to the SD. The FOR simulation produced more deep convection and rainfall over the simulation period than either of the SAV or SD simulations. The SD squall lines produced 14.0 mm per grid cell, 15.8 mm for the SAV, and 22.3 mm for the FOR. Whereas the SAV produced just 12% more than the SD, the FOR produced 37% more rainfall than the SD and 29% more than the SAV.

Given the same sounding and nearly identical initial soil moisture and temperature profiles for the three land covers, Figures 3–5 imply that, for the FOR simulation, evapotranspiration from the forest cover helped to create a moister boundary layer with a stronger vertical gradient of θ_e and more MSE. Even though the latent heat flux in the FOR (Figure 3c) between 16:00–20:00 is decreasing, it is still higher than the morning latent heat flux in the SD and would partially compensate for the reduction of MSE by convective activity. In Figure 8 at 17:00, only dissipating convection exists in the SD, whereas a second burst of development will take place within an hour in the FOR. In Figure 9, contour plots of θ_e at 17:00 for the SD and FOR, the SD vertical profile of θ_e is well mixed. In the FOR contour plot, there are large bubbles of high θ_e air, suggesting additional convection is required.

For parcels, CAPE is a useful measure of the potential for deep convection. Prior to convective initiation, 10:00–12:00, the FOR simulation has the highest CAPE at 3300 J kg^{-1} compared to 2800 J kg^{-1} for the SAV (16% less) and 2500 J kg^{-1} (25% less) for the SD. Not only does the FOR have more CAPE, it has significant CAPE (> 1000 J kg^{-1}) until 17:00, compared to 14:00 in the SAV and SD. The FOR level of free convection for rising parcels is 500 m lower in than the SAV in the morning and 1000 m lower in the afternoon. The lower the level of free convection, the weaker the triggering required, and the less energy expended by rising parcels. The larger, longer lived FOR squall lines follow from the differences in the amount and timing of MSE and CAPE between the FOR and the other simulations.

Sensitivity of Results

Thus far, we have compared the effect of changing the land cover. In the SD, SAV, and FOR simulations, there is the same, a fixed vegetation density at each gridcell. We ran

additional simulations to understand the sensitivity of our results to vegetation density, the humidity of the initial sounding, and the resolution of the grid. How does sensitivity to these factors compare to the effect of changing the land cover? For brevity's sake, we will focus on selected variables such as latent heat flux and rainfall and not repeat the full discussion of MSE, boundary layer growth, and other variables discussed earlier.

a. Sensitivity to vegetation density

We first tested the effect of vegetation density within a particular land cover type. Since "semi-desert" implies very sparse vegetation, it made sense to test just the savanna and broadleaf forest land covers. We created two variable density simulations in which we assigned a vegetation density between 10–70% to each grid point using a random number generator. The total amount of vegetation in a variable density simulation was less than in the corresponding fixed density simulation. The albedo and roughness heights were adjusted for the vegetation density specified at each cell.

Figure 10 compares the latent heat flux for the fixed and variable density simulations. From 9:00–15:00, the difference between the fixed and variable density forest simulations is 50–200 W m^{-2} compared to 30–70 W m^{-2} for the savanna simulations. Although the difference between the fixed and variable density savanna is not trivial, it is 40–60% smaller than the difference between the fixed and variable density forest. The differences in latent heat flux between the fixed and variable density simulations presage differences in squall line characteristics and rainfall. The squall lines that later develop in the variable density simulations are both smaller and shorter lived with less rainfall than in the fixed density simulations.

The water budgets in Table 3 summarize the differences among the three land covers and the fixed and variable density simulations. Along with the Figure 7 and Table 2, Table 3

confirms that significantly more condensation, evaporation, and rainfall occur in the FOR simulation compared to the SD and SAV simulations and that more condensation, evaporation, and rainfall occur in the fixed density simulations compared to the variable density simulations. The difference in rainfall volume between the fixed and variable density savanna (19%) and the fixed and variable density forest (21%) is smaller than the difference between the SAV and FOR (fixed density) simulations (29%).

The combination of vegetation type and density (SAV vs. FOR) had a more pronounced effect than changing the vegetation density alone. The FOR simulation was only slightly more efficient in converting condensate to rainfall than the other simulations. The difference in rainfall (29% vs. SAV and 37% vs. SD) is more likely a function of 2–3 g kg^{-1} additional water vapor in the FOR boundary layer (*c.f.* Figure 4c) from surface fluxes. Even the SD simulation produced more rainfall (10%) than the variable density savanna. In the afternoon, the SD latent heat flux and boundary layer humidity are higher than in the variable density savanna, and measurable rainfall ends an hour later in the SD. The change in boundary layer humidity from surface fluxes even in relatively dry, hot conditions (Table 1) in the SD was greater than the threshold sensitivity of deep convection to boundary layer humidity changes (1 g kg^{-1}) in the study by Crook (1996).

b. Sensitivity to initial sounding humidity

How does the changing the landscape and thus local evapotranspiration compare to changes in the sounding that might be caused by changes in the summer monsoon and the transport of water vapor? We conducted four additional simulations using savanna land cover in which we added 2% and 5% to the observed mixing ratios at all levels in the original sounding and then subtracted 2% and 5% from the original sounding. Inspection of sounding data from

Dakar, Senegal suggests that 2% and 5% are smaller than the variability in the West African summer monsoon. This is not an exhaustive study of sensitivity to monsoon conditions, but should provide additional insight into sensitivity to small changes in sounding humidity. Table 4 has the water budgets from these tests with the original SAV simulation for comparison. Increasing the humidity increased the rainfall by 5% and 35% for the +2% and +5% simulations, respectively. The +5% simulation using savanna land cover produced slightly more rainfall than the FOR simulation. A 5% increase in sounding humidity from large-scale flow produces a response on the same magnitude of changing the savanna vegetation to dense forest.

Decreasing the humidity has an even larger effect. Rainfall decreased by 30% and 40% for the –2% and –5% simulations, respectively. Lucas et al. (2000) suggest that decreasing the low to mid-level (up to 700 mb) humidity increases the entrainment of dry air from the environment. Increasing entrainment in the "minus" simulations appears to have significantly decreased the upward mass flux in the convective updrafts. In Table 4 the increase in condensate and precipitation efficiency in the "plus" simulations is less than the decrease in the same variables in the "minus" simulations. The surface fluxes in the "minus" simulations exacerbated the effect of a drier sounding. Whereas moist soil and a dry atmosphere might accelerate latent heat flux, compensating for a drier boundary layer, the dry soil profiles used in all our simulations resulted in stressed (supply-limited) rather than potential (demand-limited) evapotranspiration rates in the "minus" simulations. The latent heat flux decreased an average of 25% in the critical morning hours when the vertical gradient of MSE is determined and CAPE accumulates. The latent heat flux in the "plus" simulations was similar to the original SAV.

c. Sensitivity to grid resolution

As with the previous section, this is not an exhaustive sensitivity study of grid resolution in the manner of Weisman et al. (1997) who tested grid resolutions from 1–12 km. We ran simulations using our three land covers at 0.5 km and 1.5 km resolution and compared the effect on the surface physics and water budget. In the morning, the fine (0.5 km) and coarse (1.5 km) resolutions had no systematic, non-trivial effect on the surface fluxes. With latent heat fluxes the same for fine and coarse resolution land surfaces, there were no differences in the MSE per unit area or the average mixing ratio in the boundary layer. After 12:00, differences did emerge. Peak 10-cm soil temperatures were 2–4 K lower in the fine resolution simulations, and the latent (sensible) heat fluxes were higher (lower) between 12:00–18:00 in the fine resolution simulations. Although the change in W m^{-2} was largest for the FOR fine simulation, the SD fine simulation had the largest percent increase in latent heat flux, 30%, compared to the SAV, 25%, and FOR, 10%.

Shrinking the grid resolution may not have affected the morning surface physics but it noticeably affected the convective intensity and rainfall. In Weisman et al. (1997), as the horizontal scale became smaller, the resultant vertical motions for a given distance increased proportionally. Here, the maximum vertical velocities and rain rates for the fine resolution simulations (Figure 8) were as much as 50% greater than those of the coarse resolution simulations. However, the average rain rates (not shown) tended to be higher in the coarse resolution simulations. In Weisman et al., there was very little difference in the condensation, evaporation, rainfall, or precipitation efficiency and the system evolution was similar for simulations with grid resolutions 4 km or finer. For our fine simulations there was an increase in the condensation, evaporation, and rainfall. As an example, Table 5 compares the water budgets

of the coarse and fine resolution semi-desert. In Table 5, the increase in rainfall, 1.183×10^9 kg km^{-1}, for the semi-desert fine simulation (i.e., SD) is approximately the same for the other land covers, making the percent increase for the semi-desert (41%) higher than the percent increases for the savanna (33%) and broadleaf forest (24%) fine simulations. The increase in rainfall in the fine simulations fed back to the land surface in the afternoon, forcing higher latent heat flux and reducing soil heating.

The time series of maximum vertical velocities for the coarse resolution simulations (not shown) exhibited more variability than the time series for the fine grid simulations (Figure 8a). The coarse grid squall lines had a greater downshear tilt and lower precipitation efficiencies (5–10%), suggesting more interaction of the updrafts with environmental shear. The warm air ahead of the fine grid squall lines was 1–3 g kg^{-1} more moist and 2–4 K warmer compared to the coarse grid squall lines. More significantly, the cold pools behind the fine grid squall lines were 1–2 g kg^{-1} drier and 2–4 K colder. The fine grid simulations had longer periods of strong convection and thus produced a greater volume of condensate and rainfall.

Conclusion

This study used a two-dimensional coupled land/atmosphere (cloud-resolving) model to investigate the influence of land cover on the water budgets of squall lines in the Sahel. We created three different land covers, a sparsely vegetated semi-desert, a grassy savanna, and a dense evergreen broadleaf forest. For the three land covers, the sounding of 23 June 1981 from the COPT81 experiment provided the initial state of the atmosphere. The initial soil temperature and moisture profiles were warm, dry, and in equilibrium with the atmosphere. Our simulation grid was a 1000 km at 0.5 km resolution in x and 21.5 km (stretched from 80 to 1200 m) in z. All simulations began at local midnight and ran for 24 hours to capture a diurnal cycle.

The latent heat flux, boundary layer mixing ratio, and MSE in the boundary layer exhibited noticeable variations among the three land covers. The broadleaf forest had the highest latent heat flux, the shallowest, moistest, slowest growing boundary layer, and significantly more MSE per unit area than the savanna and semi-desert. The savanna had more boundary layer humidity and MSE per unit area than the semi-desert, but the difference between the savanna and semi-desert was smaller than the difference between the broadleaf forest and the savanna. Deep convection and rainfall started first in the savanna and last in the broadleaf forest. Although all simulations produced squall lines, the broadleaf forest had the most intense, longest-lived squall lines with 29% more rainfall than the savanna and 37% more than the semi-desert. Rainfall ceased by 18:00 in the savanna and semi-desert compared to 24:00 for the broadleaf forest. By 18:00, significant vertical gradients of θ_e still existed in the broadleaf forest but not in the savanna or semi-desert.

We explored the sensitivity of these results by testing the effect of vegetation density, initial sounding humidity, and grid resolution. Vegetation type determines the efficiency with which water is extracted from sub-surface soil and transpired, while vegetation density determines the surface area through which transpiration can take place. Although changing either variable by itself can affect results, the synergistic effect created by changing both at the same time resulted in greater differences in rainfall among land cover types than among simulations of the same land cover with varying amounts of vegetation. To compare the effect of changing local evapotranspiration to variability in the summer monsoon, the initial sounding humidity was varied (+/– 2% and +/– 5%) for simulations using the savanna land cover. Small changes in humidity produced large changes in the condensate and rainfall, although the increase in rainfall for the "plus" simulations was smaller than the decrease in rainfall in the "minus"

simulations. Reducing the grid resolution from 1.5 km to 0.5 km also produced noticeable increases in rainfall. At 0.5 km the cells were tilted more upright, and the cold pools were drier and colder, resulting in longer periods of strong convection and more condensate and rainfall with higher precipitation efficiencies. The differences between our fine and coarse grid simulations suggest that additional work is needed to examine the relationship between grid resolution and convective intensity in a high shear environment.

Land cover, particularly vegetation type and density, influences boundary layer characteristics and thus the environment in which convective cells develop, although variability in the African summer monsoon may obscure the signal from land cover for individual squall lines. Changes in mixing ratio by surface fluxes, however, are likely to be smaller and confined to a shallower layer than those produced by the monsoon. Given the sensitivity of convection to small changes in humidity and the potential contribution from surface fluxes, the land surface may either compensate for or exacerbate large-scale conditions, particularly in dry regimes. Recalling Nicholson (1988), land surface changes from drought and human activity may result in a lowered probability of generating squall lines capable of 40 mm of rainfall in a day. Large-scale forcing may trigger squall lines, but the condition of the boundary layer may result in a squall line on the order of the semi-desert squall line rather than the broadleaf forest squall line, that is, a weaker, shorter lived squall line with less total rainfall.

Acknowledgements

The GCE model is supported by the HQ NASA Physical Climate Program and the TRMM Project. We are grateful to Dr. R. Kakar (HQ NASA) for his support of GCE modeling research and to Pete Wetzel and Barry Lynn for GCE-PLACE coupling. Changhai Liu (NCAR) supplied the sounding used in the simulations. This work benefited from discussions with Aaron Boone, Scott Braun, Greg Jenkins, Chris Lucas, John Molinari, Chris Thorncroft, and Ed Zipser. The corresponding author received financial support from NASA Grant NGT 5-81 and the University at Albany Professional Development Fund.

References

Aspliden, C. I., Y. Tourre, and J. B. Sabine, 1976: Some climatological aspects of West African disturbance lines during GATE. *Mon. Wea. Rev.*, **104,** 1029-1035.

Baker, R. D., B. H. Lynn, A. Boone, W.-K. Tao, and J. Simpson, 2001: The influence of soil moisture, coastline curvature, and land-breeze circulations on sea-breeze initiated precipitation. *J. Hydrometeor.*, **2**, 193-211.

Betts, A. K. and J. H. Ball, 1995: The FIFE surface diurnal cycle climate. *J. Geophys. Res.*, **100,** 25679-25693.

Betts, A. K. and J. H. Ball, 1998: FIFE surface climate and site-average dataset 1987-89. *J. Atmos. Sci.*, **55,** 1091-1108.

Brubaker, K. L., D. Entekhabi, and P. S. Eagleson, 1993: Estimation of continental precipitation recycling. *J. Climate*, **6,** 1077-1089.

Chalon, J. P., G. Jaubert, F. Roux, and J. P. Lafore, 1988: The West African squall line observed on 23 June during COPT81: Mesoscale structure and transports. *J. Atmos. Sci.*, **45,** 2744-2763.

Chang, C.-Y. and M. Yoshizaki, 1993: Three-dimensional modeling study of squall lines observed in COPT81. *J. Atmos. Sci.*, **50,** 161-183.

Crook, N. A., 1996: Sensitivity of moist convection forced by boundary layer processes to low-level thermodynamic fields. *Mon. Wea. Rev.*, **124,** 1767-1786.

Dudhia, J., M. W. Moncrieff, and D. W. K. So, 1987: The two-dimensional dynamics of West African squall lines. *Quart. J. Roy. Meteor. Soc.*, **113,** 121-146.

Ferrier, B. S., W.-K. Tao, and J. Simpson, 1996: Factors responsible for precipitation efficiencies in mid-latitude and tropical squall line simulations. *Mon. Wea. Rev.*, **124,** 2100-2125.

Grabowski, W. W., X. Wu, M. W. Moncrieff, and W. D. Hall, 1998: Cloud-Resolving Modeling of Cloud Systems during Phase III of GATE. Part II: Effects of Resolution and the Third Spatial Dimension. *J. Atmos. Sci.*, **55,** 3264-3282.

Hodges, K. I. and C. D. Thorncroft, 1997: Distribution and statistics of African mesoscale convective weather systems based on the ISCCP Meteosat imagery. *Mon. Wea. Rev.*, **125,** 2821-2837.

Lafore, J.-P. and M. W. Moncrieff, 1989: A numerical investigation of the organization and interaction of the convective and stratiform regions of tropical squall lines. *J. Atmos. Sci.*, **46,** 521-544.

Lin, Y.-L., R. D. Rarley, and H. D. Orville, 1983: Bulk parameterization of the snow field in a cloud model. *J. Clim. Appl. Meteor.*, **22,** 1065-1092.

Lucas, C., E. J. Zipser, and B. S. Ferrier, 2000: Sensitivity of tropical West Pacific oceanic squall lines to tropospheric wind and moisture profiles. *J. Atmos. Sci.*, **57,** 2351-2373.

Lynn, B. H., W.-K. Tao, and P. J. Wetzel, 1998: A study of landscape generated deep moist convection. *Mon. Wea. Rev.*, **126,** 928-942.

Mohr, K. I., J. S. Famiglietti, A. Boone, and P. J. Starks, 2000: Modeling soil moisture and surface flux variability with an untuned land surface scheme: A case study from the Southern Great Plains 1997 Hydrology Experiment. *J. Hydrometeor.*, **1,** 154-169.

Mohr, K. I., J. S. Famiglietti, and E. J. Zipser, 1999: The contribution to tropical rainfall with respect to convective system type, size, and intensity estimated from the 85-GHz ice scattering signature. *J. Appl. Meteor.*, **38,** 596-606.

Nesbitt, S. W., E. J. Zipser, and D. J. Cecil, 2000: A census of precipitation features in the Tropics using TRMM: Radar, ice scattering, and lightning observations. *J. Climate*, **13,** 4087-4106.

Nicholls, M. E., R. H. Johnson, and W. R. Cotton, 1988: The sensitivity of two-dimensional simulations of tropical squall lines to environmental profiles. *J. Atmos. Sci.*, **45,** 3625-3649.

Nicholson, S. E., 1988: Land surface interaction: Physical processes and surface changes and their impact. *Prog. Phys. Geogr.*, **12,** 36-65.

Nicholson, S. E., C. J. Tucker, and M. B. Ba, 1998: Desertification, drought, and surface vegetation: An example from the West African Sahel. *Bull. Amer. Meteor. Soc.*, **79,** 815-829.

Roux, F., 1988: The West African squall line observed on 23 June during COPT81: Kinematics and thermodynamics of the convective region. *J. Atmos. Sci.*, **45,** 406-426.

Rowell, D. P. and J. R. Milford, 1993: On the generation of African squall lines. *J. Climate*, **6,** 1181-1193.

Rutledge, S. A. and P. V. Hobbs, 1984: The mesoscale and microscale structure and organization of clouds and precipitation in midlatitude cyclones. Part XII: A diagnostic modeling study of precipitation development in narrow cold frontal rainbands. *J. Atmos. Sci.*, **41,** 2949-2972.

Tao, W.-K., S. Lang, J. Simpson, C.-H. Sui, B. Ferrier, and M.-D. Chou, 1996: Mechanisms of cloud-radiation interaction in the tropics and midlatitudes. *J. Atmos. Sci.*, **53,** 2624-2651.

Tao, W.-K. and J. Simpson, 1993: Goddard Cumulus Ensemble model. Part I: Description. *Terr. Atmos. Oceanic Sci.*, **4,** 35-72.

Tao, W.-K., J. Simpson, D. Baker, S. Braun, M.-D. Chou, B. Ferrier, D. Johnson, A. Khain, S. Lang, B. Lynn, C.-L. Shie, D. Starr, C.-H. Sui, Y. Wang, and P. Wetzel, 2001: Microphysics, radiation, and surface processes in the Goddard Cumulus Ensemble (GCE) model. *Meteor. Atmos. Phys.*, in press.

Weisman, M. L., W. C. Skamarock, J. B. Klemp, 1997: The resolution dependence of explicitly modeled convective systems. *Mon. Wea. Rev.*, **125,** 527-548.

Wetzel, P. J. and A. Boone, 1995: A Parameterization for Land-Atmosphere-Cloud Exchange (PLACE): Documentation and testing of a detailed process model of the partly cloudy boundary layer over heterogeneous land. *J. Climate*, **8,** 1810-1837.

Xu, K.-M. and D. A. Randall, 1996: Explicit Simulation of Cumulus Ensembles with the GATE Phase III Data: Comparison with Observations. *J. Atmos. Sci.*, **53,** 3709–3736.

Figure and Table Captions

Figure 1. Political map of Africa. The box (dotted line) encloses the West African Sahel.

Figure 2. Pre-squall environment sounding from the COPT81 field experiment. Low-level shear from the lowest model layer to the height of the African Easterly Jet core at 605 mb is 3.5×10^{-3} s^{-1}. Mid-level shear from the height of the jet core to 6 km is -5.0×10^{-3} s^{-1}.

Figure 3. Time series of area-average surface fluxes: net radiation – ground heat flux in a), sensible heat flux in b), latent heat flux in c).

Figure 4. Time series of boundary layer characteristics. Growth curves in a) are not smooth because height is diagnosed from discrete model layers. MSE per unit area in the boundary layer in b). Area-average mixing ratio (qv) in the boundary layer in c).

Figure 5. *x-z* contour plots of θ_e at 11:00. 348 K contour is shaded dark gray, 350 K shaded light gray, 351 K shaded black.

Figure 6. Time series of total hydrometeor (cloud liquid water, rain, cloud ice, snow, graupel) mixing ratio.

Figure 7. *x-t* contour plots of rainfall rate. Contour intervals are 0.001, 5, 25, and 100 mm hr^{-1}. 5 mm hr^{-1} shaded in dark gray, 25 mm hr^{-1} in light gray, 100 mm hr^{-1} in black.

Figure 8. Time series of maximum vertical velocity in a) and maximum rain rate in b). Maximum rain rates are determined at 5 min intervals.

Figure 9. *x-z* contour plots of θ_e at 17:00 for the semi-desert and broadleaf forest. 348 K contour is shaded dark gray, 350 K shaded light gray, 351 K shaded black.

Figure 10. Time series of latent heat flux for fixed and variable density (VD) simulations.

Table 1. Selected vegetation and soil characteristics for the three land covers.

Legend: % veg. cover is the percentage of area covered by transpiring vegetation; root profile is the cumulative frequency distribution of roots in the 5 soil moisture reservoirs; surface roughness in m; minimum stomatal resistance in s m^{-1}; saturated (sat.) hydraulic conductivity in m s^{-1}.

Table 2. Comparison of areas at specified rain rates.

Note: Figures are expressed as percent differences between two land covers. That is, there is 52% more area where rainfall is greater than 0 mm hr^{-1} in the FOR simulation compared to the SD.

Table 3. Water budgets for the fixed and variable density (VD) simulations.

Table 4. Water budgets for simulations testing sensitivity to initial sounding humidity.

Note: All simulations in Table 4 used savanna (SAV) land cover.

Table 5. Comparison of water budgets for the semi-desert fine grid and coarse grid simulations.

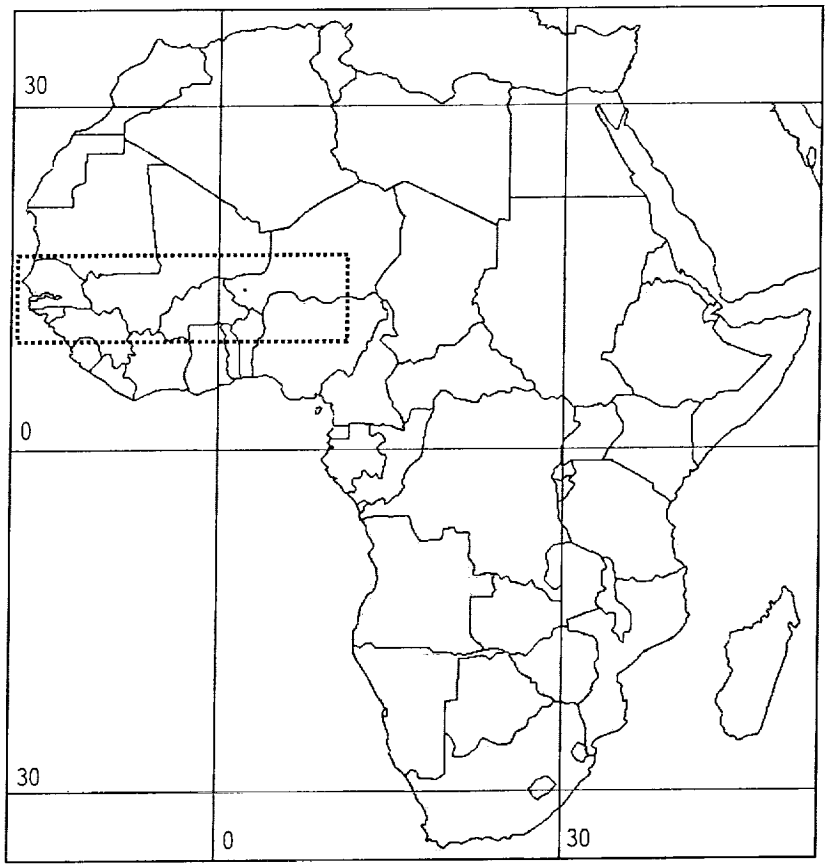

Figure 1. Political map of Africa. The box (dotted line) encloses the West African Sahel.

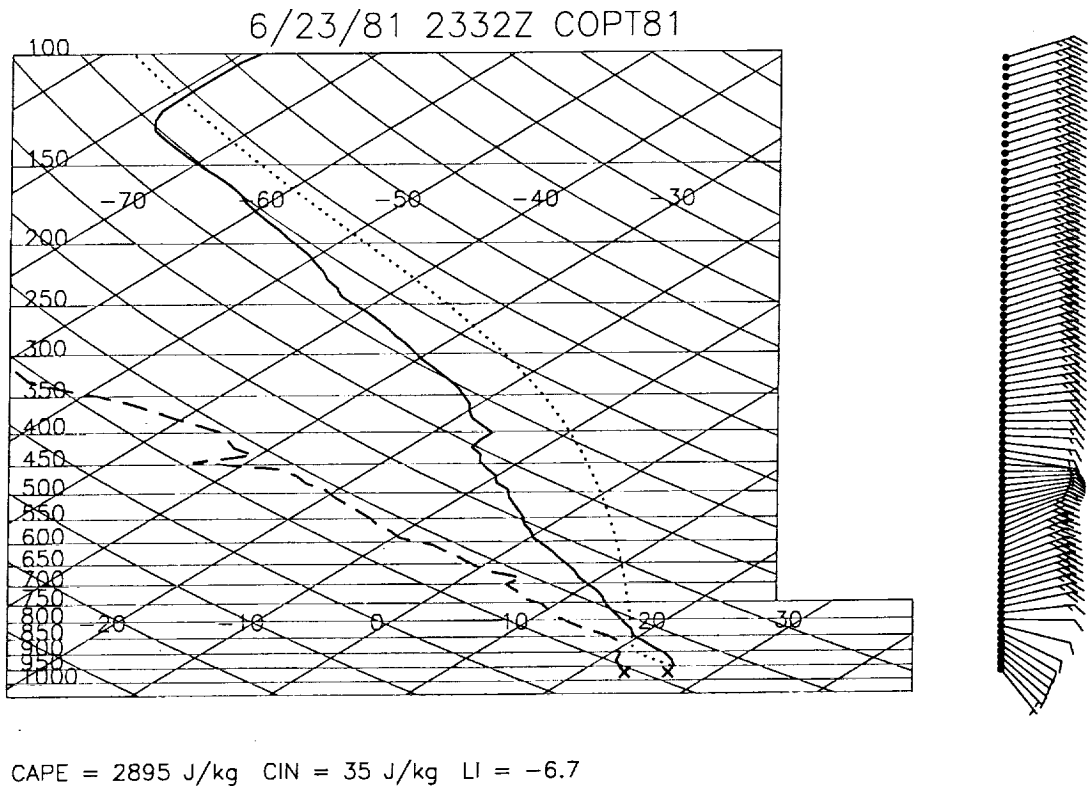

Figure 2. Pre-squall environment sounding from the COPT81 field experiment. Low-level shear from the lowest model layer to the height of the African Easterly Jet core at 605 mb is 3.5×10^{-3} s^{-1}. Mid-level shear from the height of the jet core to 6 km is -5.0×10^{-3} s^{-1}.

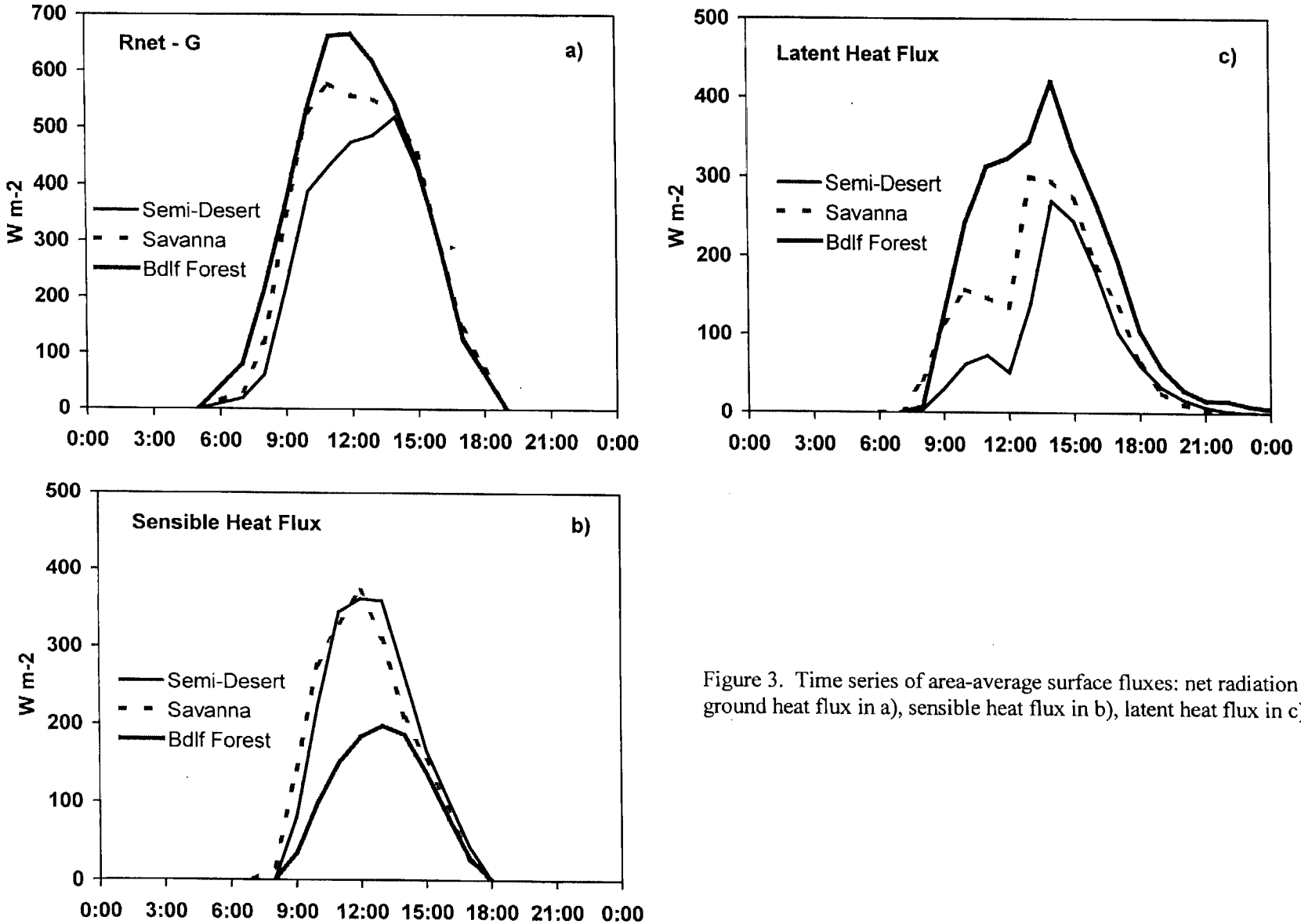

Figure 3. Time series of area-average surface fluxes: net radiation – ground heat flux in a), sensible heat flux in b), latent heat flux in c).

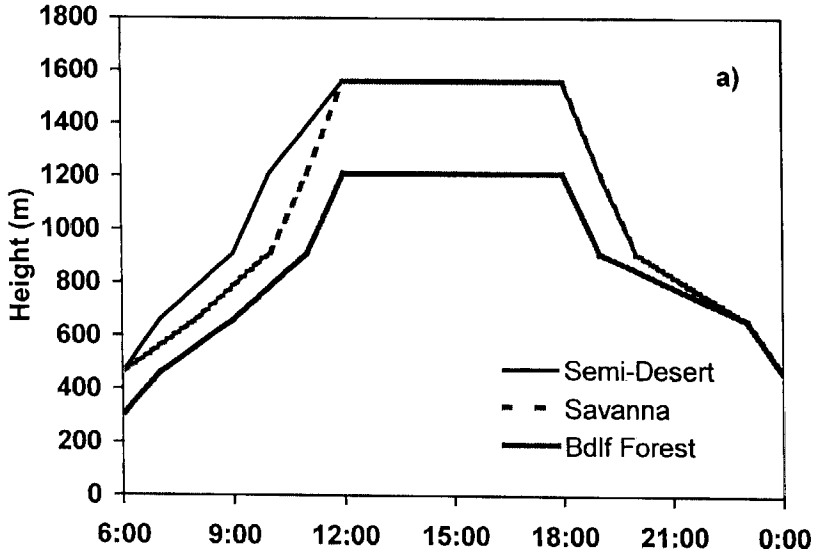

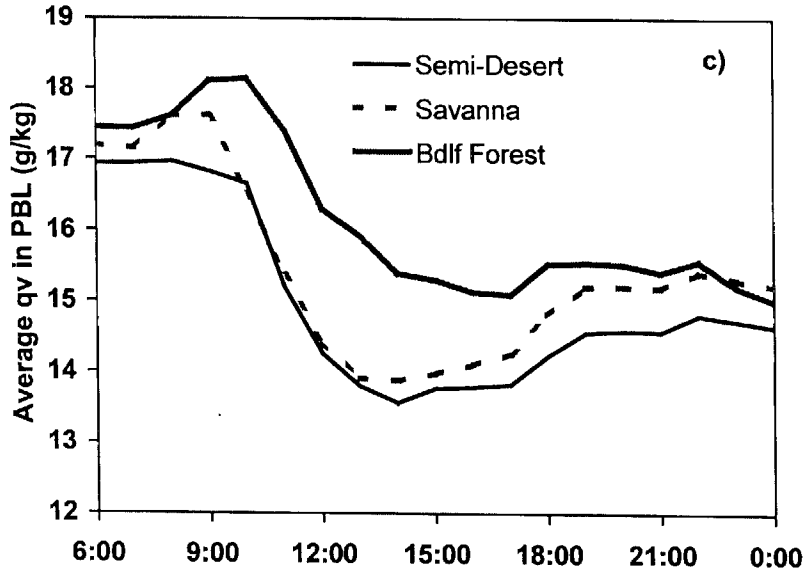

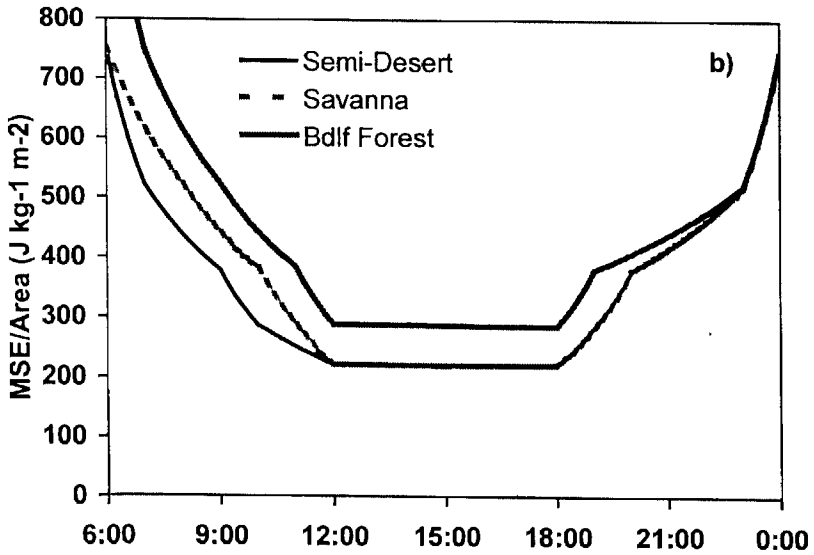

Figure 4. Time series of boundary layer characteristics. Growth curves in a) are not smooth because height is diagnosed from discrete model layers. MSE per unit area in the boundary layer in b). Area-average mixing ratio (qv) in the boundary layer in c).

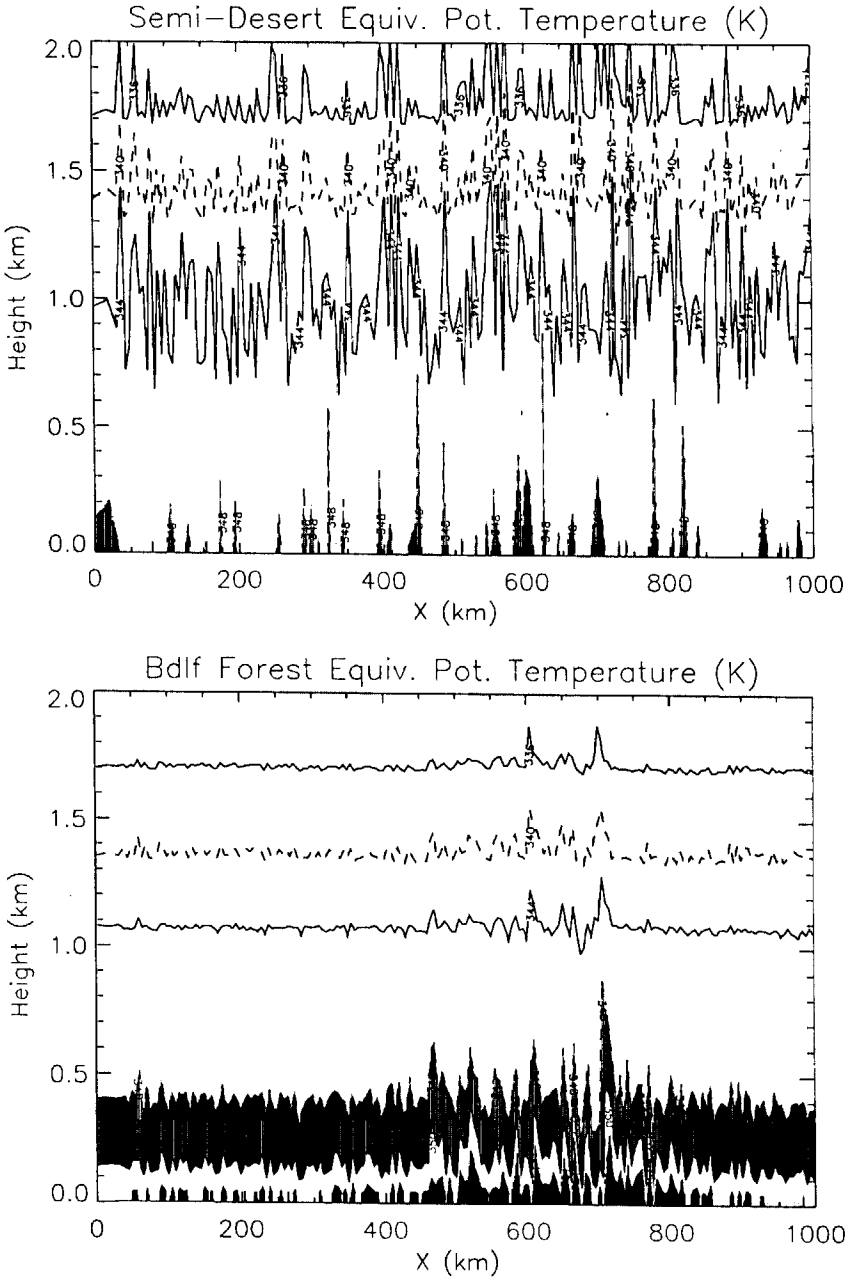

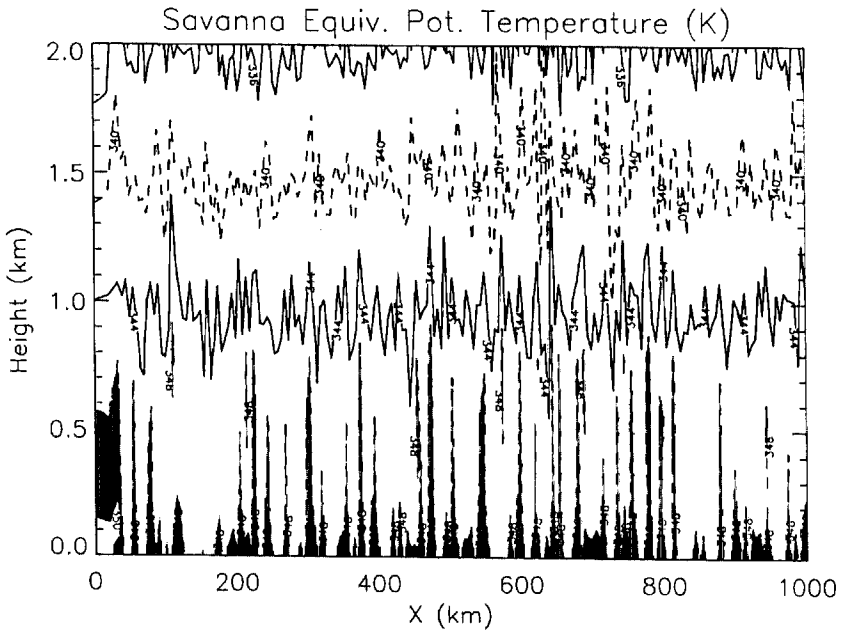

Figure 5. *x-z* contour plots of θ_e at 11:00. 348 K contour is shaded dark gray, 350 K shaded light gray, 351 K shaded black.

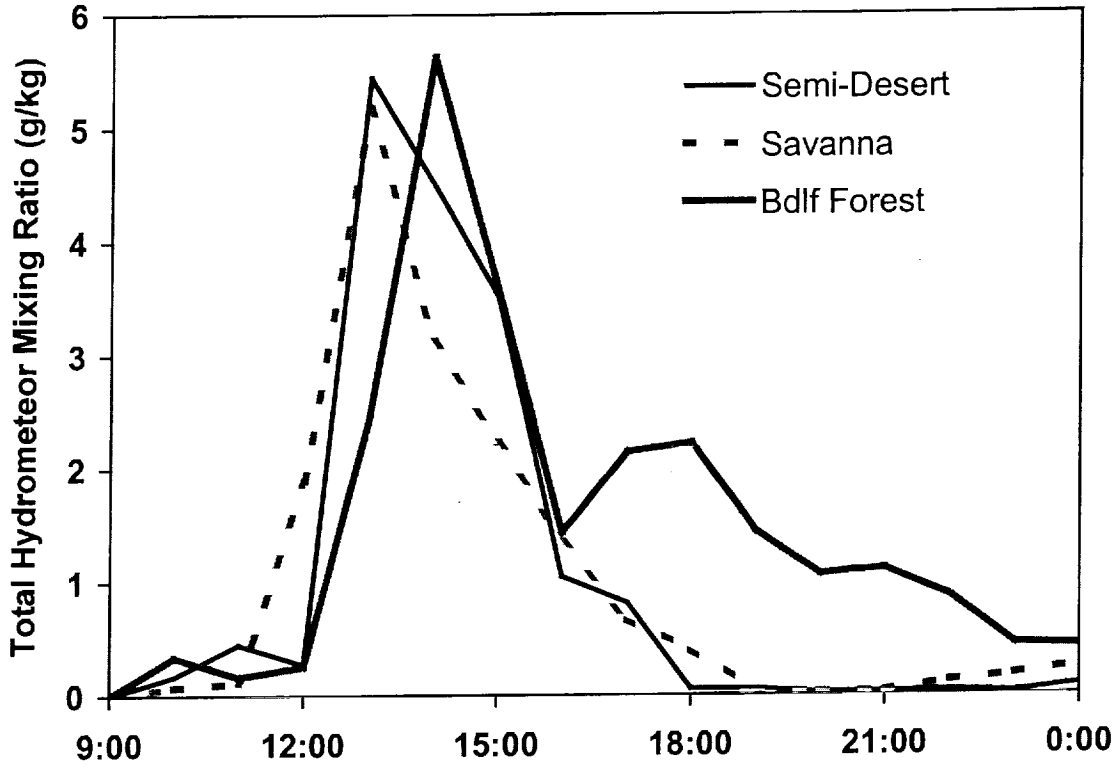

Figure 6. Time series of total hydrometeor (cloud liquid water, rain, cloud ice, snow, graupel) mixing ratio.

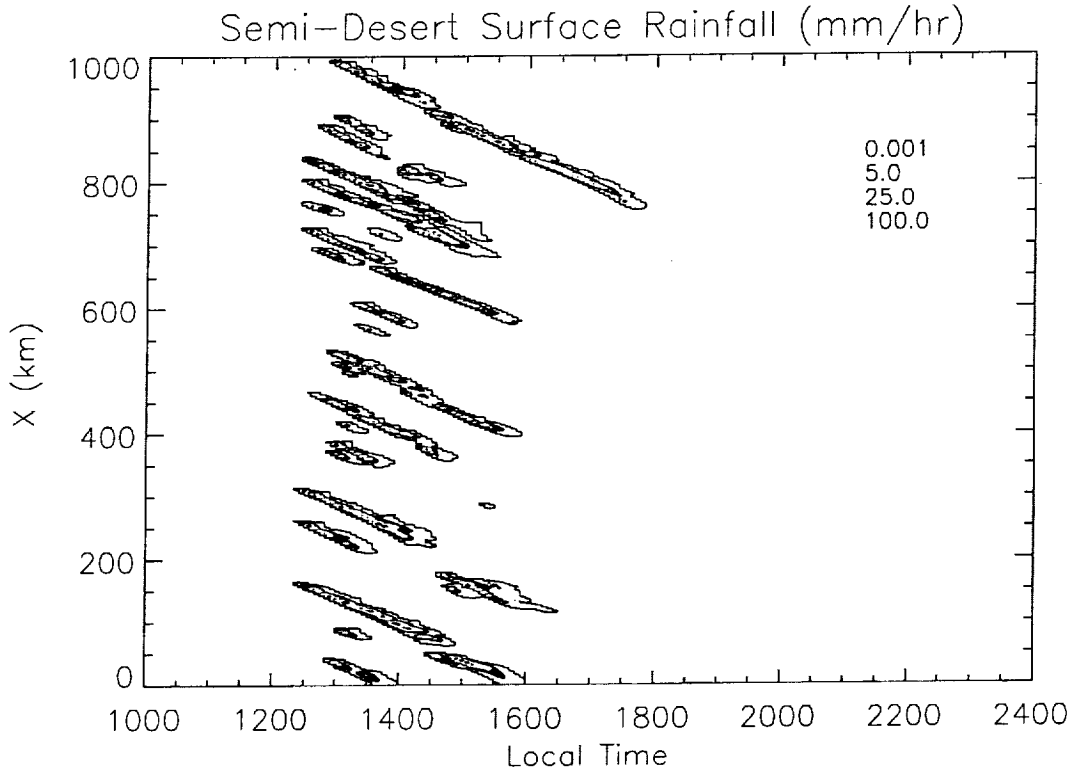

Figure 7. *x-t* contour plots of rainfall rate. Contour intervals are 0.001, 5, 25, and 100 mm hr^{-1}. 5 mm hr^{-1} shaded in dark gray, 25 mm hr^{-1} in light gray, 100 mm hr^{-1} in black.

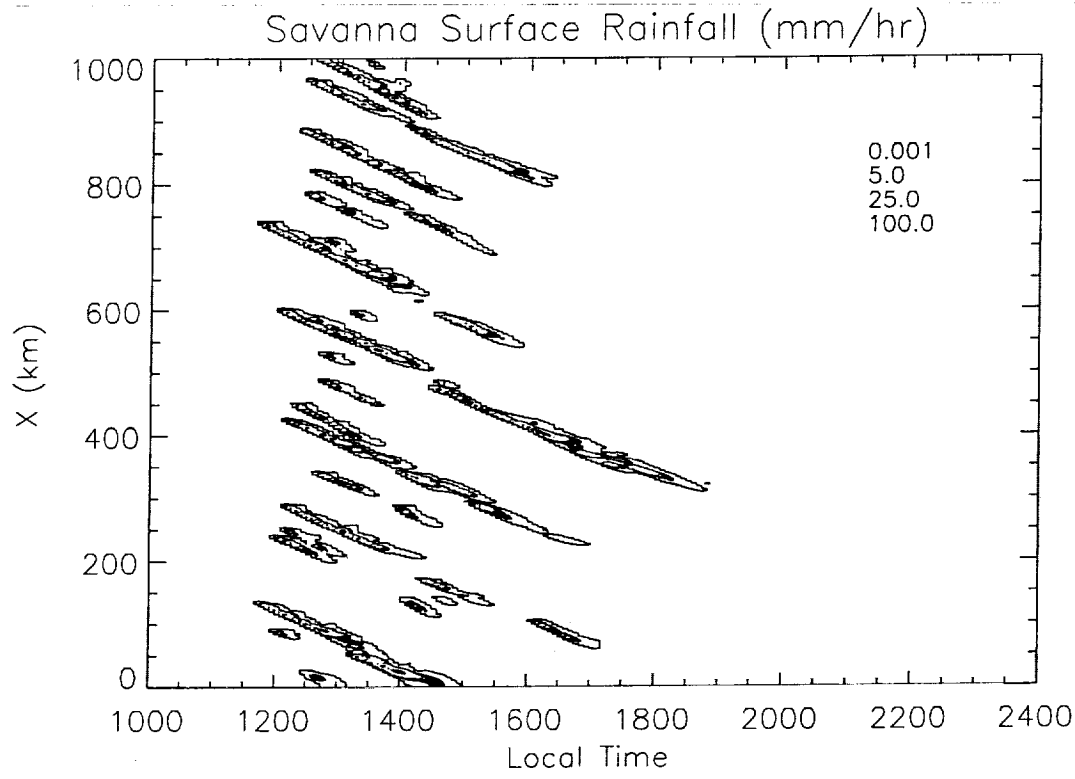

Figure 7. Continued.

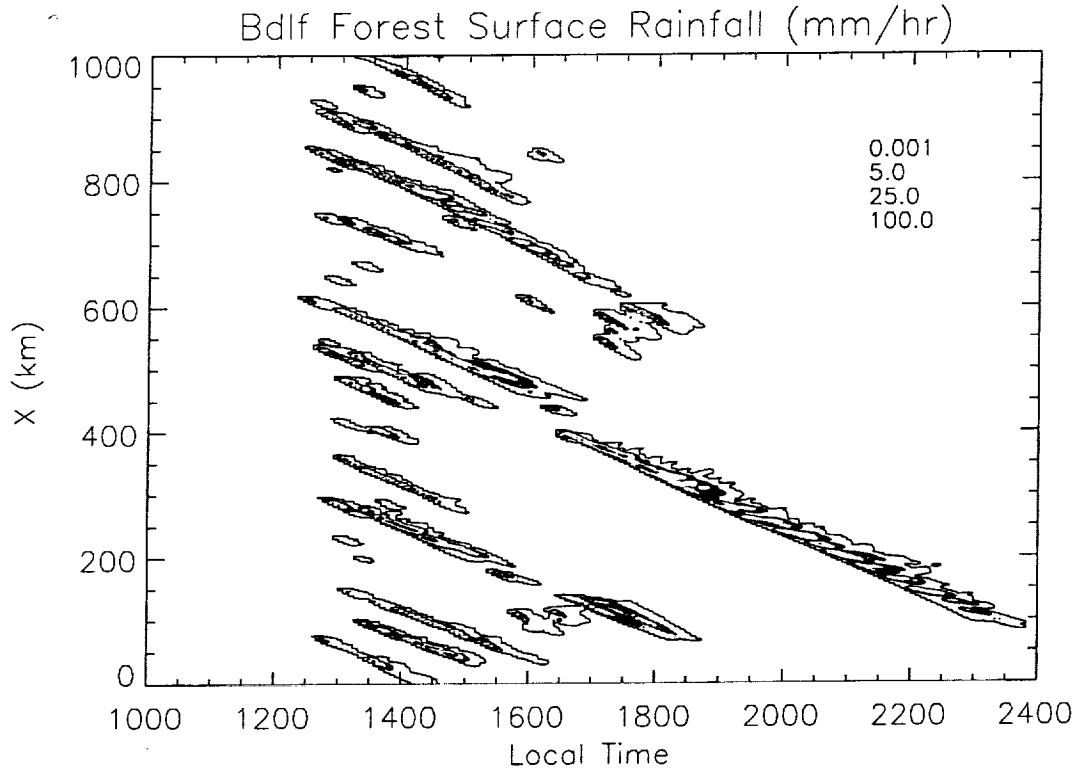

Figure 7. Continued.

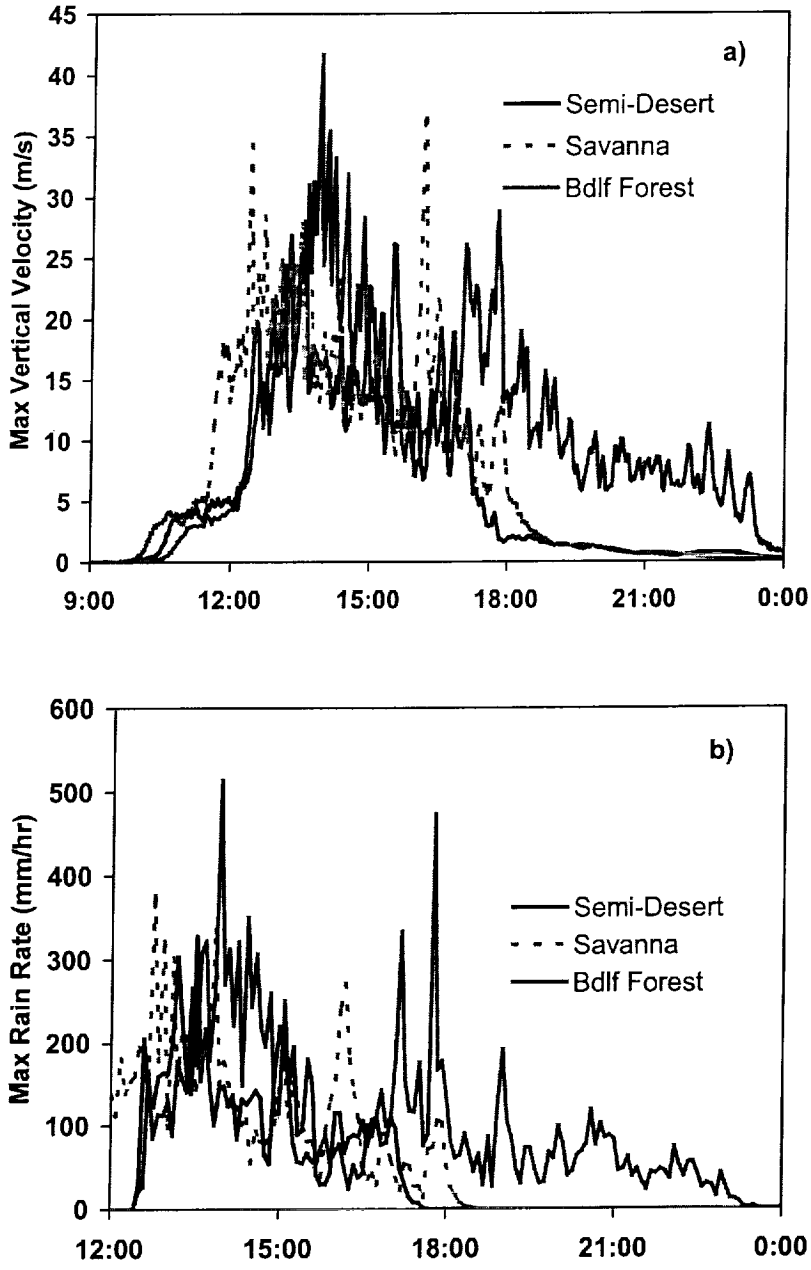

Figure 8. Time series of maximum vertical velocity in a) and maximum rain rate in b). Maximum rain rates are determined at 5 min intervals.

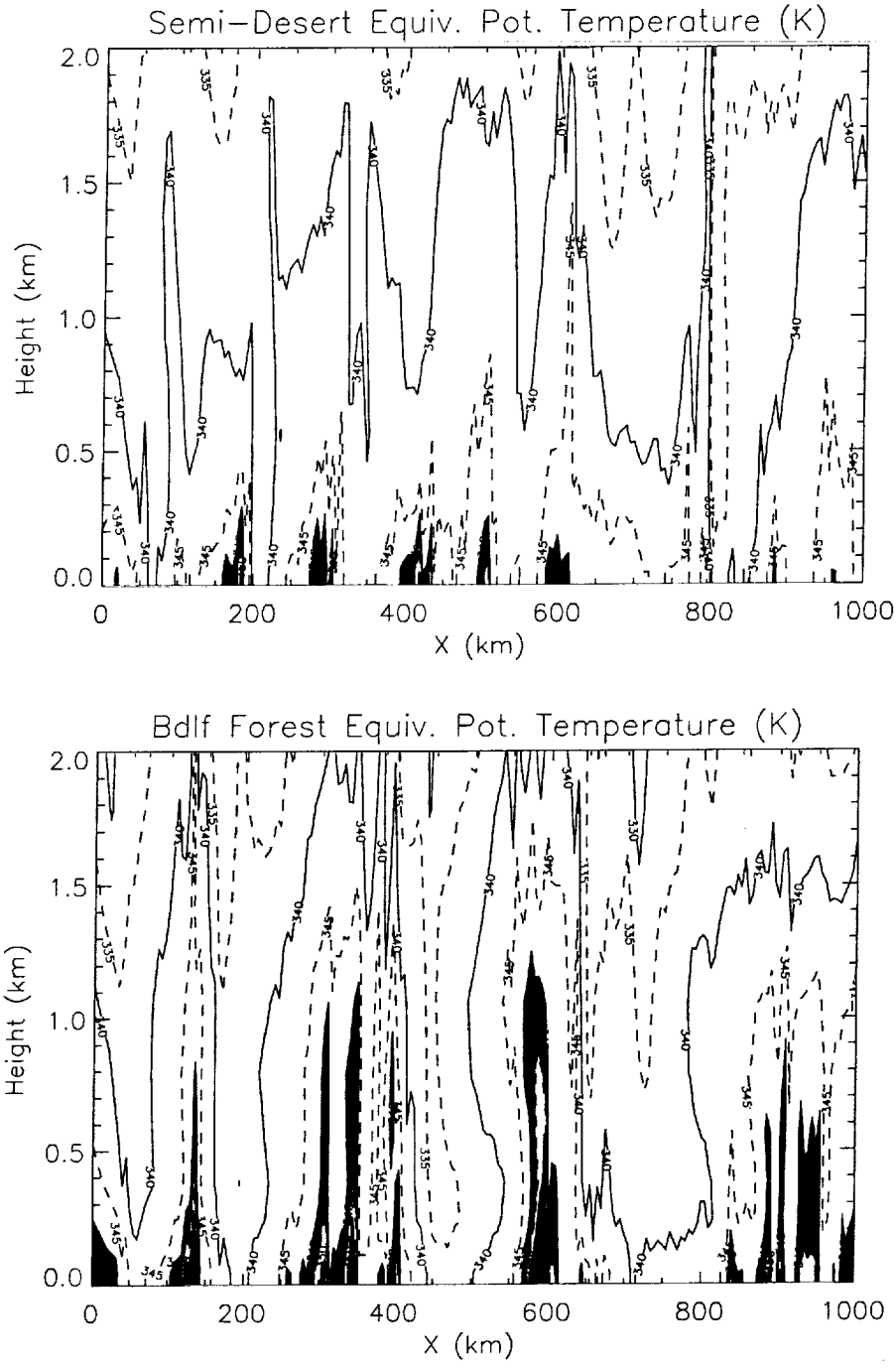

Figure 9. *x-z* contour plots of θ_e at 17:00 for the semi-desert and broadleaf forest. 348 K contour is shaded dark gray, 350 K shaded light gray, 351 K shaded black.

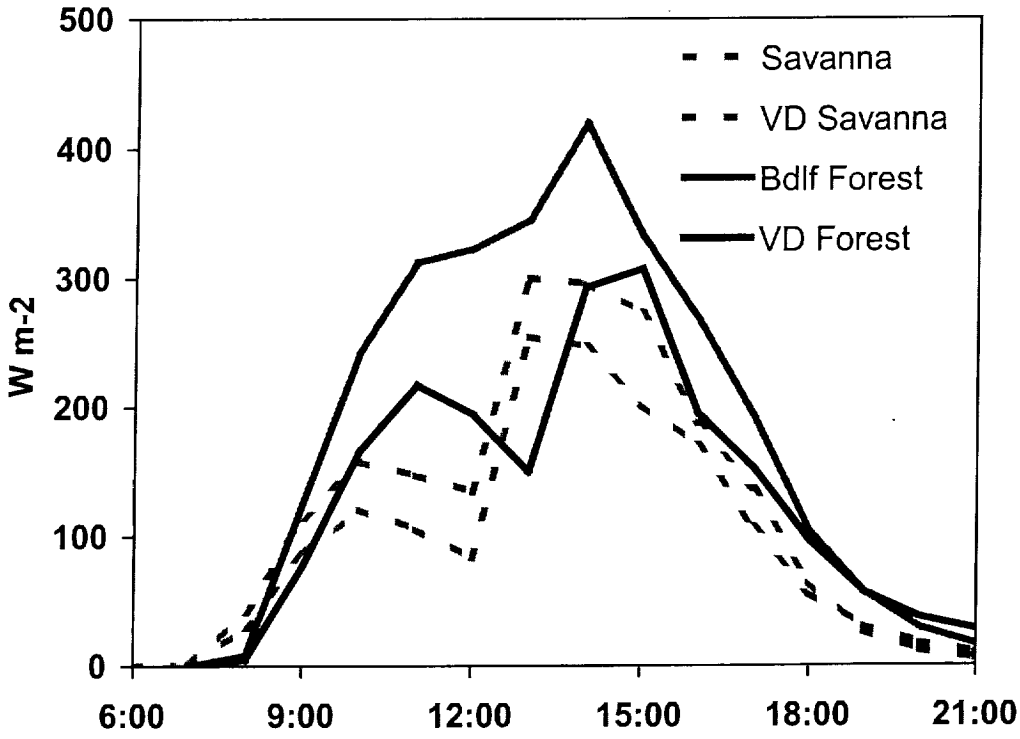

Figure 10. Time series of latent heat flux for fixed and variable density (VD) simulations.

Vegetation	Semi-Desert (SD)	Savanna (SAV)	Broadleaf Forest (FOR)	Soil	Sandy Loam
Albedo	0.25	0.18	0.14	Albedo	0.20
% Veg. Cover	20%	50%	70%	Porosity	0.40
Leaf Area Index	0.40	2.0	3.75	Sat. Hydraulic Conductivity	0.00122
Root Profile	0.0	0.0	0.0	Initial Soil	5–10%
Layers 1–5	0.20	0.25	0.25	Moisture	7–12%
	0.25	0.50	0.50	Layers 1–5	12–18%
	0.50	0.25	0.25		15–20%
	0.05	0.0	0.0		18–20%
Surface Roughness	0.20	1.0	1.0	% Silt	20%
Min. Stomatal Resistance	110	110	80	% Sand	70%
				% Clay	10%

Table 1. Selected vegetation and soil characteristics for the three land covers.

Legend: % veg. cover is the percentage of area covered by transpiring vegetation; root profile is the cumulative frequency distribution of roots in the 5 soil moisture reservoirs; surface roughness in m; minimum stomatal resistance in s m^{-1}; saturated (sat.) hydraulic conductivity in m s^{-1}.

Rain Rate (mm hr^{-1})	FOR vs. SD	FOR vs. SAV	SAV vs. SD
> 0	52%	47%	9%
5	45%	40%	8%
10	44%	37%	11%
25	35%	31%	6%
50	30%	22%	10%
> 100	31%	22%	12%
Total	48%	43%	9%

Table 2. Comparison of areas at specified rain rates.

Note: Figures are expressed as percent differences between two land covers. That is, there is 52% more area where rainfall is greater than 0 mm hr^{-1} in the FOR simulation compared to the SD.

Water Budget ($\times 10^8$ kg km^{-1})	Semi-Desert	Savanna	Bldf. Forest	VD Bdlf. Forest	VD Savanna
Suspended Condensate	0.04	0.06	0.19	0.05	0.04
Total Condensate (C)	84.38	93.30	118.90	98.48	80.60
Total Evaporation	54.38	59.35	72.65	61.75	52.95
Rain (R)	28.61	32.47	45.47	35.86	26.21
Precipitation Efficiency (R/C)	34%	35%	38%	36%	33%

Table 3. Water budgets for the fixed and variable density (VD) simulations.

Water Budget ($\times 10^8$ kg km^{-1})	**Savanna**	**+2%**	**+5%**	**–2%**	**–5%**
Suspended Condensate	0.06	0.09	0.18	0.05	0.01
Total Condensate (C)	93.30	96.78	122.45	75.73	68.05
Total Evaporation	59.35	60.78	71.50	51.70	48.53
Rain (R)	32.47	34.50	49.36	22.98	18.66
Precipitation Efficiency (R/C)	35%	36%	40%	30%	27%

Table 4. Water budgets for simulations testing sensitivity to initial sounding humidity.

Note: All simulations in Table 4 used savanna (SAV) land cover.

Water Budget ($\times 10^8$ kg km^{-1})	Semi-Desert Fine	Semi-Desert Coarse
Suspended Condensate	0.04	0.08
Total Condensate (C)	84.38	65.41
Total Evaporation	54.38	49.06
Rain (R)	28.61	16.78
Precipitation Efficiency (R/C)	34%	26%

Table 5. Comparison of water budgets for the semi-desert fine grid and coarse grid simulations.